An Analytical Model for the Triaxial Compressive Stress-strain Relationships of Cemented Pasted Backfill (CPB) with different curing time

Zhanguo Xiu[1†], Shuhong Wang[1✉], Yingchun Ji[2], Feili Wang[3†], Fengyu Ren[1]

[1]School of Resources and Civil Engineering, Northeastern University, China.

[2]School of Science, Engineering & Environment, University of Salford, UK.

[3]College of Science, Qingdao University of Technology, China.

[✉]Corresponding Author: wangshuhong@mail.neu.edu.cn

[†]Co-first author: Feili Wang

Highlights

- Triaxial compressive tests of CPB with different curing time were carried out.
- A damage constitutive model was proposed using the experimental measurements.
- The proposed model can predict the stress-strain relationships with good accuracy.

Abstract

The strength of CPB is gradually enhanced with the increase of curing time. It is of great significance to study the stress-strain behaviors of CPB with different curing time under triaxial loading conditions. The triaxial compressive tests of CPB samples with 4 different curing time (1, 3, 7, and 28 days) were firstly conducted using GCTS (*Geotechnical Consulting ＆ Testing System*) loading system under 4 different lateral constraint ratios (σ_3/UCS≈0%, 10%, 20%, and 30%). The experimental data were then used to develop a damage constitutive model in which the lateral constraint rations σ_3/UCS plays a key role. The tested stress-strain curves from the experiments were used to verify the proposed damage constitutive model. The comparisons between the tests and the model prediction showed that the triaxial strength of CPB can be accurately predicted by the Mohr-Coulomb strength criterion. An obvious secondary elastic strengthening stage was identified in the stress-strain curves of CPB when σ_3/UCS is high (≥20%). And the proposed damage constitutive model can accurately represent the stress-strain relationships of CPB with different curing time and σ_3/UCS. The results presented in this study contribute to a better understanding of the triaxial mechanical behaviors of CPB.

Keywords: Tailings; Cemented paste backfill; Constitutive model; Triaxial compressive test; Stress-strain curve

1 Introduction

Backfilling mining voids using solid waste (e.g., tailings, waste rock, etc.) as main materials is not only beneficial to the environment but also effective to increase productivity and ensure safety [1-3]. CPB is widely used as a backfilling material due to its excellent working performance [4, 5]. CPB (as a cement-based material) backfilled into the underground mined-out areas gradually hardens with the curing time to resists the deformation of the surrounding rock walls. Therefore, the mechanical behaviors of CPB can be regarded as an important foundation for the backfilling design and application.

The stress-strain relationship (of represented as a constitutive model or stress-strain model) is one of the main indicators that can reflect the mechanical behaviors (e.g., peak stress, peak strain, and elastic modulus, etc.) of solid materials. Establishing a suitable constitutive model to describe the stress-strain relationship is necessary to fully understand the stress-strain evolution process. For backfilling materials under uniaxial compression, existing constitutive models consider various factors, such as: solid content [6-8], cement-tailing ratios [7, 9, 10], layered structure of tested sample [10-12], porosity and pore size [14], etc. In addition, different loading methods were also added to some of the existing constitutive models to describe the tested stress-strain curves, such as: creep behaviors [15-17], thixotropic [18], and cyclic loading [19], etc. There were also constitutive models in which the complex storage environments of the backfilled CPB and the multi-physics coupling were considered [20-22].

For backfilled CPB structures on site, the mechanical properties of CPB units located at a given depth were also significantly affected by the lateral constraint stress (σ_3) Therefore, the triaxial mechanical properties of CPB need to be better understood. Moreover, the triaxial stress-strain relationship of CPB is also an important indicator of triaxial mechanical properties. To describe the triaxial stress-strain relationship, an experimental study on CPB samples with curing time of 28 and 91 days was conducted by Fall et al. [23]. The research established the relationships between deviator stress, elastic modulus, peak strain, and lateral constraint stress. Liu et al. [24] developed a numerical model to reproduce the stress-strain curves of CPB based on the PFC^{2D} software. Fu et al. & Yang et al. [25, 26] performed a series of triaxial compression tests to investigate the stress-strain curves of CPB with different solid content.

For the above-mentioned studies, the established constitutive models of CPB were mostly based on the stress-strain curves obtained by the uniaxial compressive tests. However, for the triaxial mechanical behaviors of the CPB, although some related experimental studies and numerical analyses have been carried out, there are few reports on developing constitutive models that can accurately describe the stress-strain relationships of CPB samples under triaxial loading conditions. This work aims to develop a constitutive model using the triaxial experimental curves of CPB under different curing time. It is hoped that the damage constitutive model proposed in this work can accurately describe the triaxial stress-strain relationships under triaxial compression. The calculation method of model parameters was detailed, and, and the experimental data were also used to further demonstrate the accuracy and reliability of the proposed damage constitutive model in this study.

2 Experimental Materials and Methods

2.1 Materials and equipment

Usually, the fresh CPB slurry is mainly composed of tailings, binders, and water. The Ordinary Portland Cement (P.O. 42.5) was often selected as a binder, which is widely used in practice. To avoid the effects of uncertain reactive minerals in the nature tailings (NT) on the mechanical behaviors of CPB, artificial tailings (AT) was used to represent the NT [27-29]. The AT was composed of 99.8% SiO_2, its scanning electron microscope (SEM) image and particle size distribution curve were shown in Fig. 1. From Fig. 1a, the particle size distribution of the used AT is close to the average of 7 random mines NT in China. And for the two curves shown in Fig. 1b, the contents of fine particles (<20 μm) are 41.96% (for AT) and 39.07%

(for NT), respectively. Therefore, the used AT can be regarded as fine-grained soils [30]. More detailed information and discussions of the used AT can be found in previous studies [31, 32].

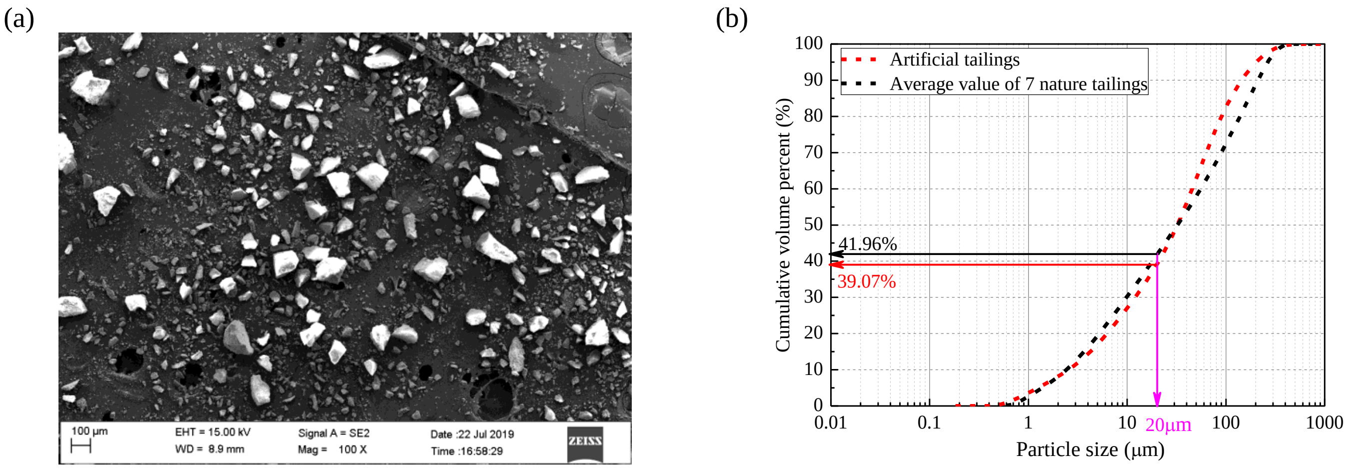

Fig.1 The relevant information about the mentioned tailings: (a) SEM image of AT (magnified 100 times); (b) the particle size distribution curves of AT and the average of 7 mines NT.

To investigate the effects of the lateral constraint stress on the mechanical behaviors of CPB, the GCTS triaxial testing system was used to conduct the experiment in this study. This testing system can provide the maximum output confining pressure (σ_3) of 1 MPa. The loading unit of the GCTS was shown in Fig. 2. For a more detailed description of this testing facility equipment, please refer to the early studies [33].

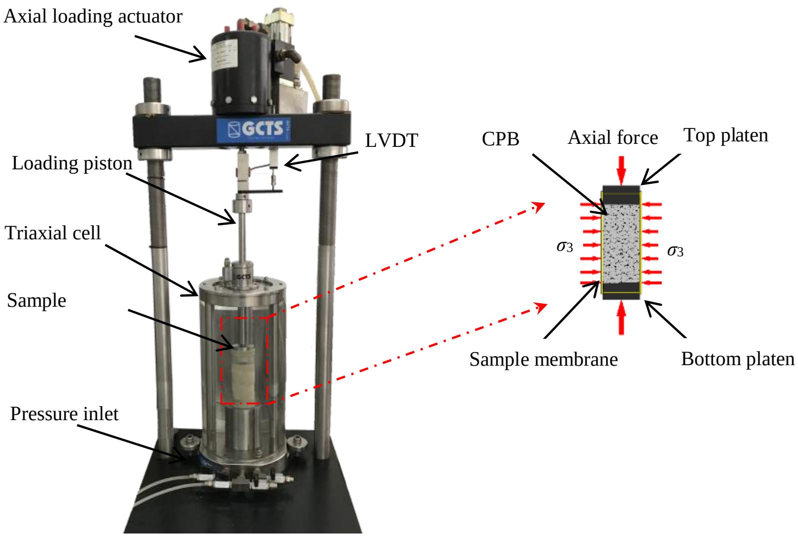

Fig.2 The GCTS triaxial testing system

2.2 Sample preparation and experimental scheme

In the experimental study, the fresh CPB slurry was composed of AT, cement type of P.O. 42.5, and tap water. The three types of materials were firstly stirred in a mortar mixer for 10 minutes to obtain a uniform CPB slurry. And for the fresh slurry, it has 75 wt.% solid content, 7.55 wt.% cement content, and a water-cement ratio (w/c) of 4.75. Then the slurry was poured into a plastic mold and cured in a temperature-controlled curing box at 20℃±2℃ for 1, 3, 7, and 28 days (shown in Table 1). Finally, after completing the planned curing process, CPB samples with Φ=50 mm and h=100 mm were prepared for further tests using the GCTS triaxial testing system.

To obtain the triaxial mechanical behaviors of the CPB, all the prepared samples with curing time of 1, 3, 7, and 28 days were subjected to the triaxial compression tests under 4 different lateral constraint ratios (σ_3/*UCS*). The unconfined compressive strength (*UCS*) tests of the CPB samples with different curing time were firstly carried out to examine the lateral constraint ratios σ_3/*UCS*. Then, the ratios between σ_3 and *UCS* (σ_3/*UCS*) were roughly set around 0%, 10%, 20%, and 30%, respectively. For the loading rate, the axial displacement of 1 mm/min (1 %/min for the tested CPB samples with the high of 100 mm in this study) was used by the displacement-controlled method. And the maximum axial strain was 12 mm (or 12% of the sample high). The detailed experimental plans and testing conditions were shown in Table 1.

Table 1. The detailed experimental plans and testing conditions

Solid content, $S_{wt.\%}$ (%)	Binder content, $B_{wt.\%}$ (%)	*w*/*c* ratio	Curing time (days)	Lateral constraint ratios (σ_3/*UCS*, %)
75%	7.55	4.75	1	0, 10.05, 20.10, 30.14
75%	7.55	4.75	3	0, 9.63, 19.07, 28.71
75%	7.55	4.75	7	0, 9.97, 19.93, 29.90
75%	7.55	4.75	28	0, 10.03, 20.05, 30.08

Note: $S_{wt\%}$ = 100%*(M_{binder}+$M_{dry\text{-}tailings}$)/M_{total}; $B_{wt\%}$ = 100%*M_{binder}/$M_{dry\text{-}tailings}$. Where, M_{binder} is the mass of cement; $M_{dry\text{-}tailings}$ is the mass of dry tailigs; M_{total} is the mass of fresh CPB slurry; σ_3 is the confining pressure; *UCS* is the peak stress under σ_3=0 kPa.

3 Experimental Results

Fig. 3 shows the triaxial tested results of the CPB samples (with Φ=50 mm and h=100 mm) under 4 different curing time (1, 3, 7, and 28 days) and 4 different lateral constraint ratios (σ_3/*UCS*≈0%, 10%, 20%, and 30%). From Fig. 3a, it is clear that the peak deviator stresses (S_d) of CPB samples with different curing time (T) are linearly increased with the increase of σ_3/*UCS*. The linear relationships between S_d and σ_3/*UCS* for samples at different curing time are represented by the fitting formulas in Fig. 3a, and the S_d at a given σ_3/*UCS* (i.e., 0%, 10%, 20%, and 30%) can be calculated using these fitting formulas. Fig. 3b shows the relationships between S_d and curing time under different lateral constraint ratios of σ_3/*UCS*. It is evident from Fig. 3b that the increase of S_d with samples at different curing time under a particular lateral constraint ratio of σ_3/*UCS* can be well fitted by a power function.

Also, the ultimate axial strain (ε_u) (refer to the axial strain when the stress-strain curve reaches the peak stress) is another key index for the triaxial mechanical behaviors of CPB. Fig. 3c shows the relationship between σ_3/*UCS* and ε_u where ε_u is exponentially increased with the increase of σ_3/*UCS*. However, ε_u is seen to be less sensitive to curing time, samples prepared with different curing time show similar ε_u values at specific lateral constraint ratios of σ_3/*UCS*.

(a) (b)

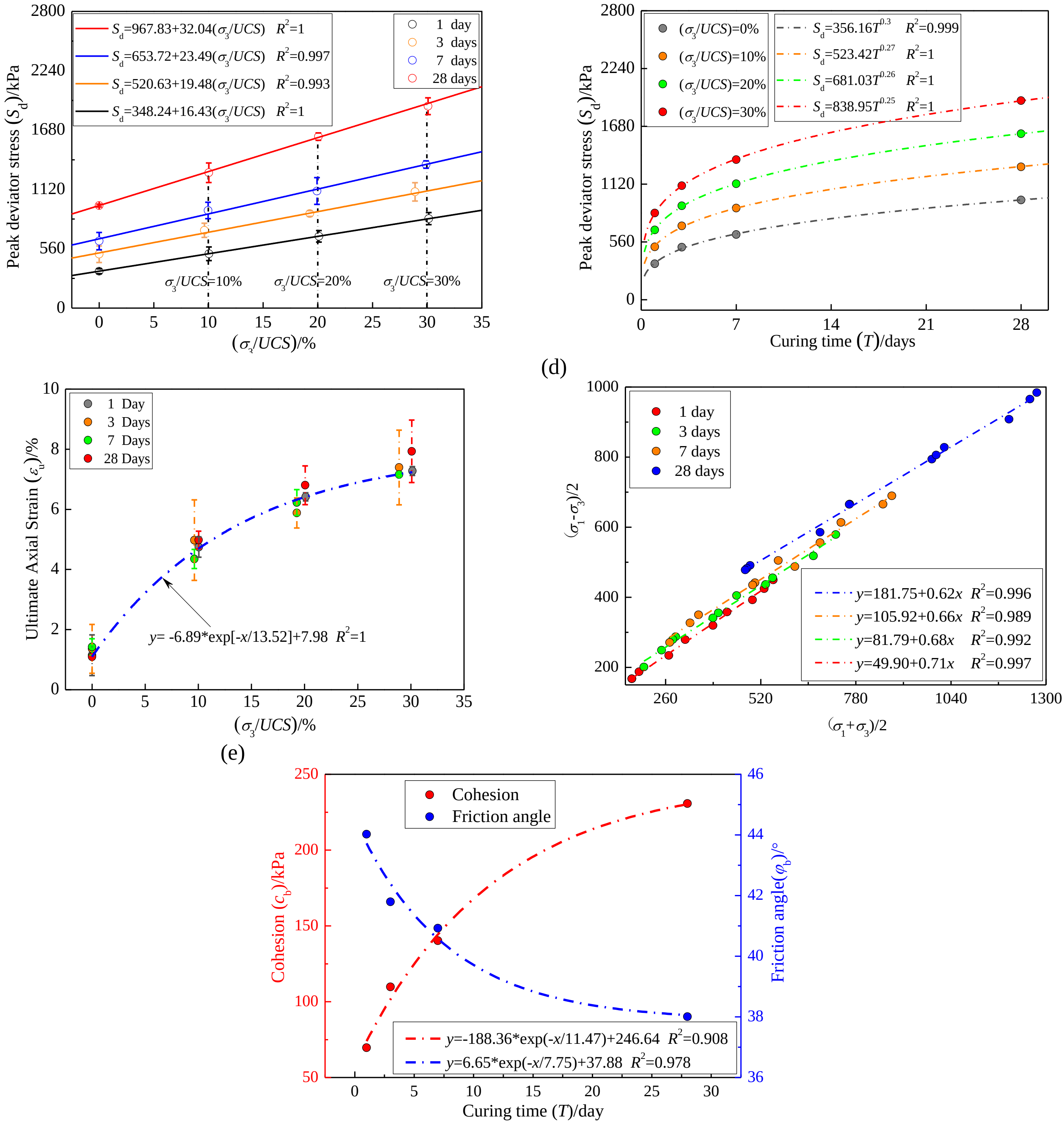

Fig. 3 The triaxial tested results of CPB samples under 4 different curing time (1, 3, 7, and 28 days) and 4 different lateral constraint ratios (σ_3/UCS≈0%, 10%, 20%, and 30%): (a) relationships between σ_3/UCS and S_d under different curing time; (b) relationships between curing time and S_d under the different σ_3/UCS; (c) relationship between ε_u and σ_3/UCS; (d) relationships between $(\sigma_1+\sigma_3)/2$ and $(\sigma_1-\sigma_3)/2$; (e) relationships between curing time and shear parameters (refer to cohesion c_b and friction angle φ_b) of CPB.

Following the research from Li et al. [34], the tested results of the CPB samples with different curing time can be described by the Mohr-Coulomb strength criterion, as:

$$\frac{\sigma_1-\sigma_3}{2}=\frac{\sigma_1+\sigma_3}{2}\sin\varphi_b+c_b\cos\varphi_b \quad (1)$$

Where σ_1 is the maximum/first principal stress; σ_3 is the minimum/third principal stress; c_b and φ_b are the cohesion and friction angle of the CPB, respectively.

According to the triaxial tested results, the relationships between $(\sigma_1+\sigma_3)/2$ and $(\sigma_1-\sigma_3)/2$ of CPB samples under different curing time were shown in Fig. 3d. Furthermore, combining Eq. 1 with the formulas fitted using the tested results (the relationships between x: $(\sigma_1+\sigma_3)/2$ and y: $(\sigma_1-\sigma_3)/2$) shown in Fig. 3d, the shear mechanical parameters (i.e., friction angle φ_b and cohesion c_b) of the CPB under the different curing time can be calculated. Fig. 3e shows the relationships between the shear mechanical parameters of the CPB and the curing time (T), where the cohesion c_b shows an obvious exponential increase and the friction angle φ_b shows an exponential decrease with the increase of curing time.

4 Stress-strain Constitutive Model and its Illustrative Examples

CPB is a heterogeneous artificial geological material, which contains many micro-defects (e.g., micro-pores and micro-cracks). The inherent defects of CPB can be considered as the damage units will significantly affect the triaxial mechanical behaviors (especially for the stress-strain relationship). Statistics from the related study show that the micro-pore size distribution inside the CPB is closely related to the Weibull distribution function [14]. Therefore, it is feasible to use the statistical method to establish a damage constitutive model.

There is an assumption that the CPB sample is composed of many micro-units. The strength (F) of the micro-unit inside the CPB sample is a random variable and satisfies the Weibull distribution function, whose probability density function $P(F)$ can be formulated by [35, 36]:

$$P(F)=\begin{cases}\dfrac{m}{F_0}\left(\dfrac{F}{F_0}\right)^{m-1}\exp\left[-\left(\dfrac{F}{F_0}\right)^m\right] & F\geq 0\\ 0 & F<0\end{cases} \tag{2}$$

Where m and F_0 are the shape parameter and scale parameter, respectively.

Assuming a CPB sample contains a total of N micro-unit, and under a certain loading condition, the number of damaged micro-unit is N_f. Then, the corresponding damage variable (D) can be expressed as:

$$D=\frac{N_f}{N} \tag{3}$$

Therefore, the number of damaged micro-units can be represented by $NP(F)\mathrm{d}F$, when the strength of micro-units increased from F to F+dF. In other words, the mathematical denotation of the number of damaged micro-units N_f can be obtained when the strength of micro-units increased from 0 to F:

$$N_f=\int_0^F NP(F)dF=N\left\{1-\exp\left[-(\frac{F}{F_0})^m\right]\right\} \tag{4}$$

Substitution of Eq. 4 into Eq. 3, damage variable (D) can be obtained:

$$D=\frac{N_f}{N}=1-\exp\left[-\left(\frac{F}{F_0}\right)^m\right] \tag{5}$$

From Eq. 5, the damage variable (D) is closely related to the strength (F) of micro-units. How to determine F is the key to solving the damage variable (D). Li et al. [37] suggested that the strength criteria of tested materials in the form of stress can be regarded as a potential method. Based on the experimental data obtained in this study, the Mohr-Coulomb strength criterion is suitable for describing the triaxial strength of CPB samples. Therefore, the strength (F) of micro-units of CPB in this study can be expressed as:

$$F=\frac{\sigma_1^*-\sigma_3^*}{2}-\frac{\sigma_1^*+\sigma_3^*}{2}\sin\varphi_b-c_b\cos\varphi_b \tag{6}$$

Furthermore, according to the damage mechanics, σ_1^* and σ_3^* of the damaged micro-units can be expressed as:

$$\sigma_1^*=\sigma_1/(1-D) \tag{7a}$$

$$\sigma_3^*=\sigma_3/(1-D) \tag{7b}$$

According to the Hooke's law:

$$\sigma_1=E\varepsilon_1(1-D)+2\mu\sigma_3 \tag{8}$$

Where E, μ, and ε_1 are the Young's modulus, Poisson's ratio, and axial strain, respectively.

Eq. 8 can be rearranged as:

$$1-D=\frac{\sigma_1-2\mu\sigma_3}{E\varepsilon_1} \tag{9}$$

Substitution of Eq. 9 into Eqs. 7a and 7b, it can be obtained:

$$\sigma_1^*=\sigma_1\left[\frac{E\varepsilon_1}{\sigma_1-2\mu\sigma_3}\right] \tag{10a}$$

$$\sigma_3^*=\sigma_3\left[\frac{E\varepsilon_1}{\sigma_1-2\mu\sigma_3}\right] \tag{10b}$$

Substitution of Eqs. 10a and 10b into Eq. 6, then, the strength (F') of micro-units with Mohr-Coulomb strength criterion can be obtained:

$$F'=\frac{E\varepsilon_1\left(\sigma_1-\sigma_3\frac{1+\sin\varphi_b}{1-\sin\varphi_b}\right)}{\sigma_1-2\mu\sigma_3}-\frac{c_b\cos\varphi_b}{1-\sin\varphi_b} \tag{11}$$

Substituting the micro-units strength (F', Eq. 11) into Eq. 5, the damage variable (D) of CPB with the Mohr-Coulomb strength criterion can be obtained:

$$D=\begin{cases}1-\exp\left[-\left(\frac{F'}{F_0}\right)^m\right] & F'\geq 0\\ 0 & F'<0\end{cases} \tag{12}$$

Finally, Substituting Eq. 12 into Eq. 8, the damage constitutive model of CPB can be given:

$$\sigma_1=\begin{cases}E\varepsilon_1\exp\left[-(\frac{F'}{F_0})^m\right]+2\mu\sigma_3 & F'\geq 0\\ E\varepsilon_1+2\mu\sigma_3 & F'<0\end{cases} \tag{13}$$

Determination of parameters (F_0 and m) is the key problem to applying this proposed constitutive model (Eq. 13). The boundary conditions at the extremum point (ε_u, σ_m) of tested triaxial stress-strain curves can be used to determine the model parameters. which is:

$$\left.\frac{d\sigma_1}{d\varepsilon_1}\right|_{\substack{\sigma_1=\sigma_m\\ \varepsilon_1=\varepsilon_u}}=0 \tag{14a}$$

$$\sigma_m=\sigma_1\Big|_{\substack{\sigma_1=\sigma_1\\ \varepsilon_1=\varepsilon_u}}=E\varepsilon_u\exp\left[-(\frac{F_m'}{F_0})^m\right]+2\mu\sigma_3 \tag{14b}$$

Solving Eqs. 14a and 14b, the model parameters F_0 and m can be evaluated by:

$$m = -\frac{AF_m^{'}}{(1-D_m)\ln(1-D_m)} \tag{15a}$$

$$F_0 = \frac{F_m^{'}}{[-\ln(1-D_m)]^{1/m}} \tag{15b}$$

In which the corresponding notations A, D_m, and $F_m^{'}$ in Eqs. 15a and 15b can be calculated by:

$$A = \frac{(\sigma_m - 2\mu\sigma_3)^2}{(E\varepsilon_u)^2\left(\sigma_m - \sigma_3\dfrac{1+\sin\varphi_b}{1-\sin\varphi_b}\right)} \tag{16a}$$

$$D_m = 1 - \frac{\sigma_m - 2\mu\sigma_3}{E\varepsilon_u} \tag{16b}$$

$$F_m^{'} = F^{'}\Big|_{\substack{\sigma_1=\sigma_m \\ \varepsilon_1=\varepsilon_u}} \tag{16c}$$

According to the triaxial experimental data obtained in this study, the fitting relationships between *UCS* (refer to the peak stress with σ_3=0 or σ_3/UCS=0%, shown in Fig. 3b), ε_u (shown in Fig. 3c), c_b & φ_b (shown in Fig. 3e) and the different curing time (T) can be given:

$$UCS = 356.16T^{0.3} \tag{17a}$$

$$\varepsilon_u = -6.89\exp[-\sigma_3/(13.52UCS)] + 7.98 \tag{17b}$$

$$c_b = -188.36\exp\left(-\frac{T}{11.47}\right) + 246.64 \tag{17c}$$

$$\varphi_b = 6.65\exp\left(-\frac{T}{7.75}\right) + 37.88 \tag{17d}$$

Substituting Eqs. 17a~17d into Eq. 13, the curing time (T) can then be taken into account by the damage constitutive model. To verify the applicability of the proposed damage constitutive model (Eq. 13), the stress-strain curves obtained in this study were taken as illustrative examples. Fig. 4(a-h) shows the comparison between the calculated stress-strain curves using the proposed damage constitutive model and the typical stress-strain curves obtained in this experimental study.

(a)

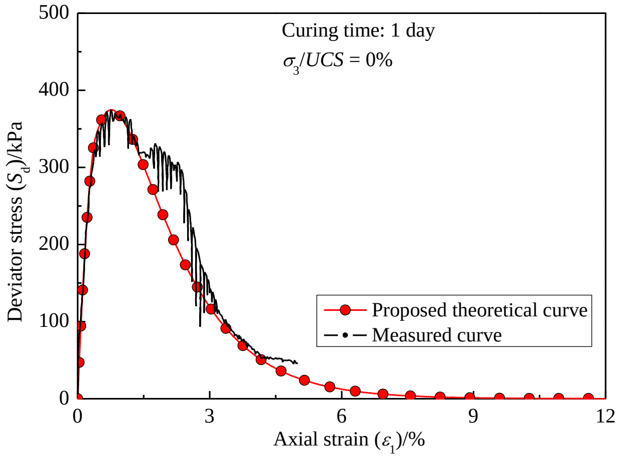

(b)

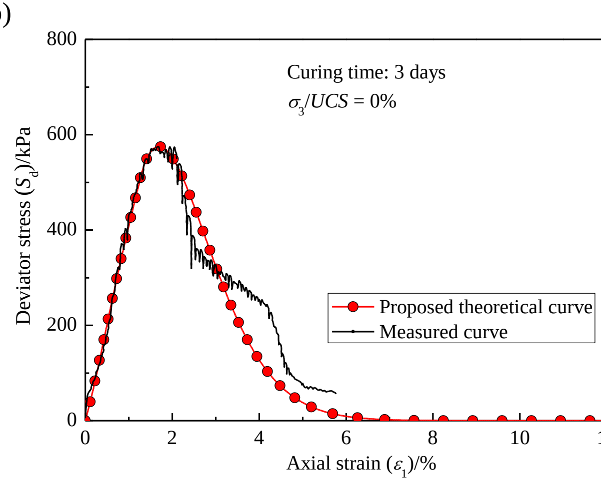

(c)

(d)

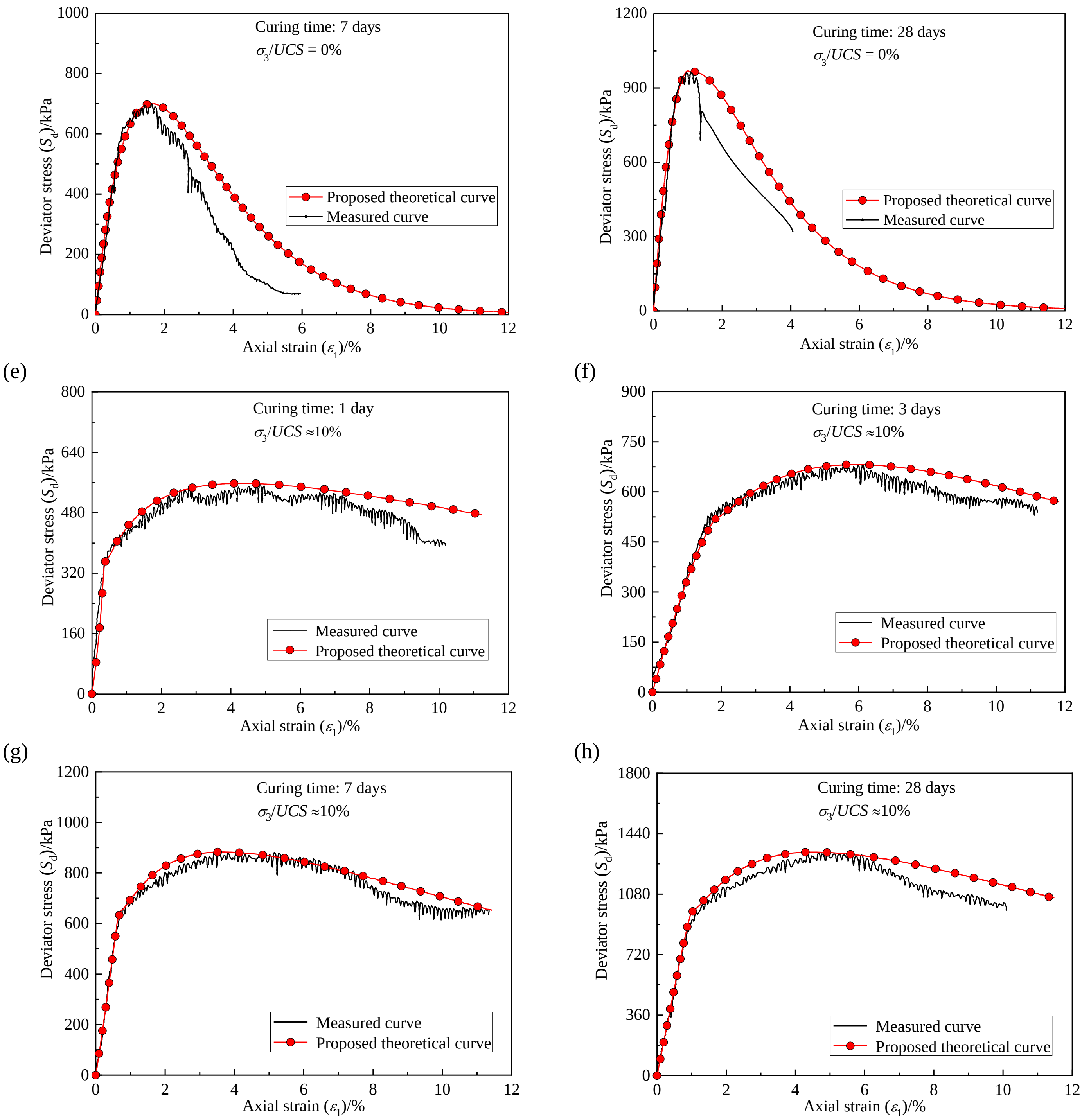

Fig.4 Comparison between experimental measurements and the proposed damage constitutive model predictions at different curing time: when $\sigma_3/UCS\approx0\%$: (a) T=1 day, (b) T=3 days, (c) T=7 days, (d) T=28 days; when $\sigma_3/UCS\approx10\%$: (e) T=1 day, (f) T=3 days, (g) T=7 days, (h) T=28 days.

Fig. 4 indicates that the results calculated by the proposed damage constitutive model agreed favorably with the experimental measurements from the CPB samples at different curing time. However, when the lateral constraint ratios σ_3/UCS is 20% or above, the discrepancies between the tested results and the proposed damage constitutive model predictions are more obvious. Taking the tested results for the CPB sample with curing time of 1 day as an example, the tested results show an obvious secondary elastic strengthening stage (as shown in Fig. 5) before the stress-strain curves reach the peak stress point (ε_u, σ_m). The same type of stress-strain curve (with an obvious secondary elastic strengthening stage) has also been observed in early studies [23, 25, 26] with the triaxial experiments when the lateral constraint ratios σ_3/UCS are higher than 20%. Due to the existence of the secondary elastic strengthening stage in the measured stress-strain curves in Fig. 5, the difference between the theoretical results using the proposed damage constitutive model and the measured curves (when $\sigma_3/UCS \geq 20\%$) can not be ignored. Therefore, it is necessary to refine the proposed damage constitutive model in order to improve its accuracy when the lateral constraint ratios are 20% or higher.

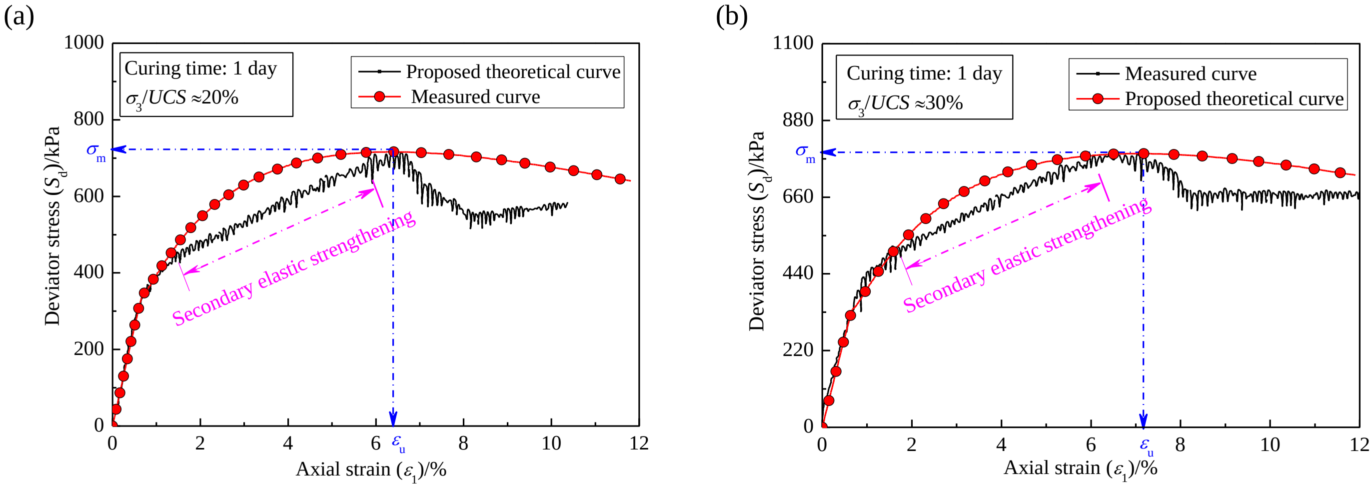

Fig. 5 Comparison between experimental and proposed theoretical curves of CPB with curing time of 1 day under $\sigma_3/UCS \geq 20\%$: (a) T=1 day and $\sigma_3/UCS \approx 20\%$; T=1 day and $\sigma_3/UCS \approx 30\%$.

To improve the damage constitutive model, the key factor is to determine the critical axial strain (ε_c, point of separation between the theoretical and experimental curves, shown in Fig. 6) at which the stress-strain curve enters the secondary elastic strengthening stage. Fig. 6 shows the values of the ultimate axial strain ε_u （when σ_3/UCS=0%） and the critical axial strain ε_c (when $\sigma_3/UCS \geq 20\%$) according to the triaxial tested data in this study. From Fig. 6, the values of ε_u and ε_c are close to each other (the relative margins of difference can be calculated by $(\varepsilon_u-\varepsilon_c)/\varepsilon_u$, which are within ±15%). Therefore, the average of ε_u and ε_c is used as a critical point of axial strain. At this critical point, the stress-strain curves under higher σ_3/UCS (≥20%) enters the secondary elastic strengthening stage. It is worth noting that the critical point of axial strain is derived from the experimental data, independent from σ_3/UCS and curing time (T), and can be regarded as a constant in this study ($\varepsilon_c \approx 1.25\%$ shown in Fig. 6).

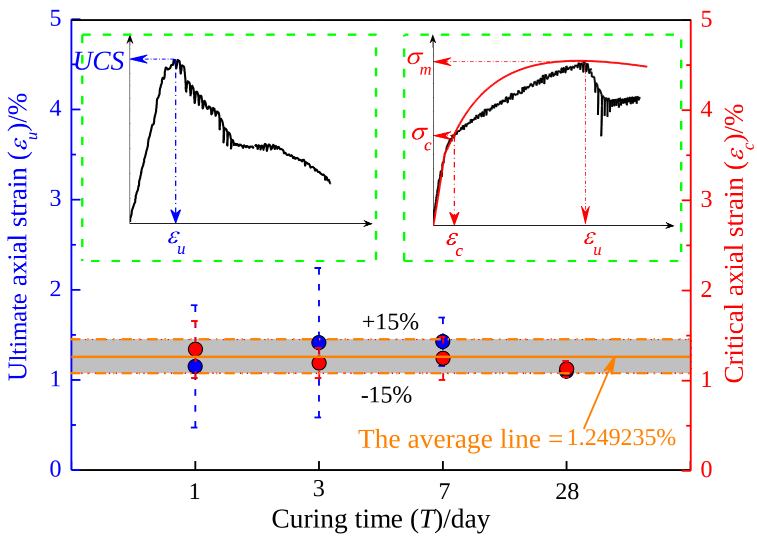

Fig. 6 The values of ultimate axial strain (ε_u) when σ_3/UCS=0% and critical axial strains (ε_c) when $\sigma_3/UCS \geq 20\%$.

After the stress-strain curve of CPB enters the secondary elastic strengthening stage, the strength (F^*) of micro-units conforms to the Hooke's law. Therefore, the F^* can be expressed as:

$$F^* = E\varepsilon_1 - \sigma_1 \tag{18}$$

The corresponding damage constitutive relationship entering the secondary elastic strengthening stage can be described as:

$$\sigma_1 = E\varepsilon_1(1-D) \tag{19}$$

Substituting Eq.12 to Eq.19, the damage constitutive model of the secondary elastic strengthening stage can be obtained:

$$\sigma_1 = \begin{cases} E\varepsilon_1 \exp\left[-(\dfrac{F^*}{F_c})^a\right] & F^* > 0 \\ 0 & F^* \le 0 \end{cases} \tag{20}$$

Also, the extremum point (ε_u, σ_m) of tested triaxial stress-strain curves was used to determine the model parameters a and F_c:

$$\left.\frac{\mathrm{d}\sigma_1}{\mathrm{d}\varepsilon_1}\right|_{\substack{\sigma_1=\sigma_m-\sigma_c \\ \varepsilon_1=\varepsilon_u-\varepsilon_c}} = 0 \tag{21a}$$

$$\sigma_m - \sigma_c = E(\varepsilon_u - \varepsilon_c)\exp\left[-(\frac{F_m^*}{F_c})^a\right] \tag{21b}$$

Combined Eq. 21a and 21b, the model parameters F_c and a can be solved as:

$$a = -\frac{F_m^*}{E(\varepsilon_u-\varepsilon_c)\ln\left(\dfrac{\sigma_m-\sigma_c}{E(\varepsilon_u-\varepsilon_c)}\right)} \tag{22a}$$

$$F_c = \frac{F_m^*}{\left[-\ln\left(\dfrac{\sigma_m-\sigma_c}{E(\varepsilon_u-\varepsilon_c)}\right)\right]^{1/a}} \tag{22b}$$

Where

$$F_m^* = F^*\Big|_{\substack{\sigma_1=\sigma_m-\sigma_c \\ \varepsilon_1=\varepsilon_u-\varepsilon_c}} \tag{23}$$

Then, the damage constitutive model entering the secondary elastic strengthening stage is added to Eq. 13, then the final damage constitutive model of the CPB can be obtained:

$$\sigma_1 = \begin{cases} \left.\begin{array}{ll} E\varepsilon_1 \exp\left[-(\dfrac{F^{'}}{F_0})^m\right] + 2\mu\sigma_3 & F^{'} \ge 0 \\ E\varepsilon_1 + 2\mu\sigma_3 & F^{'} < 0 \end{array}\right\} & \sigma_3/UCS < 20\% \\ \left.\begin{array}{ll} E\varepsilon_1 \exp\left[-(\dfrac{F^{'}}{F_0})^m\right] + 2\mu\sigma & 0 \le \varepsilon_1 < \varepsilon_c \\ \sigma_c + E(\varepsilon_1-\varepsilon_c)\exp\left[-(\dfrac{F^*}{F_c})^m\right] & \varepsilon_c < \varepsilon_1 \end{array}\right\} & \sigma_3/UCS \ge 20\% \end{cases} \tag{24}$$

The triaxial experimental curves with higher σ_3/UCS (≥20%) of CPB samples at different curing time were used to verify the accuracy of the proposed damage constitutive models. Fig. 7(a-h) shows the comparison between the theoretical stress-strain curves calculated by Eq. 24 (the secondary elastic strengthening stage was considered in the proposed damage model, blue line in these figures) & Eq. 13 (proposed damage model without secondary elastic strengthening stage, red line in these figures) and measured curves of CPB with different curing time.

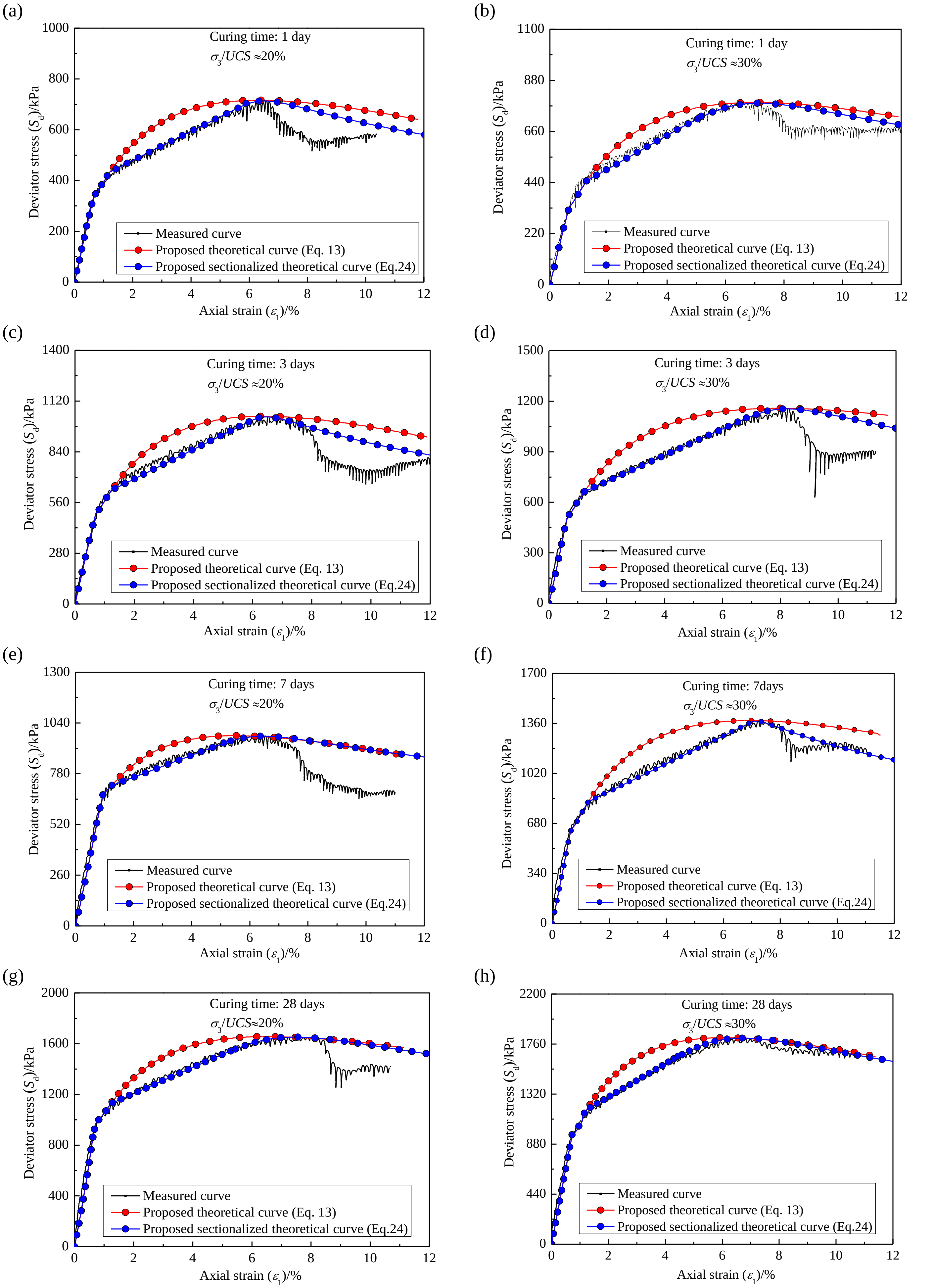

Fig. 7 Comparison between the theoretical stress-strain curves obtained by Eq. 24 & Eq. 13 and experimental curves of CPB with different curing time under higher σ_3/UCS (≥20%): (a) T=1 day and σ_3/UCS≈20%; (b) T=1 day and σ_3/UCS≈30%; (c) T=3 days and σ_3/UCS≈20%; (d) T=3 days and σ_3/UCS≈30%; (e) T=7 days and σ_3/UCS≈20%; (f) T=7 days and

σ_3/UCS≈30%; (g) T=28 days and σ_3/UCS≈20%; (h) T=28 days and σ_3/UCS≈30%.

From the comparisons shown in Fig. 7(a-h), the revised damage constitutive model (Eq. 24) can predict the stress-strain behaviors with obvious secondary elastic strengthening stage of CPB samples under higher σ_3/UCS (≥20%). And the calculated theoretical results are in good agreement with the experimental data obtained from this study, particularly before the peak deviator stress.

For cross comparison purpose, triaxial experimental results of CPB (with curing time of 28 days and cement content of 7 wt.%) from Fall et. al.' [23] were also used to verify the proposed damage constitutive model (Eq. 24) in this work. Fig. 8 shows the comparison between the experimental measurements from Fall et. al. and theoretical curves calculated by Eq.24 at different σ_3/UCS. The theoretical curves agreed with the experimental results well in general, which provides further evidence for the robustness of the proposed damage constitutive model in predicting the stress-strain relationships of CPB under different σ_3/UCS at different curing time. Due to the stress-strain curves obtained by Fall et. al.' [23] tests without obvious stress drop after reaching the peak deviator stress, the theoretical results calculated by the proposed damage constitutive model are unexpectedly more agreed with Fall et. al.' [23] tested data than the experimental results in this study. The reason for this phenomenon may be the difference in the size or material composition of the tested CPB samples.

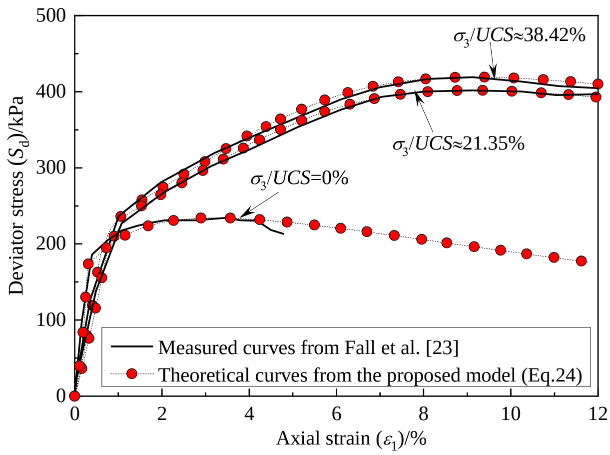

Fig. 8 Comparison between the experimental measurements (Fall et al., [23]) and theoretical curves calculated by Eq. 24 at different σ_3/UCS.

5 Conclusions

In this study, the triaxial compressive tests were performed on CPB samples with different curing time and lateral constraint ratios. Using the experimental results, a damage constitutive model was subsequently established to describe the stress-strain relationships of CPB under the given experimental conditions. The main conclusions of this research are as follows:

- The tested triaxial strength of CPB under different curing time is suitable to apply the Mohr-Coulomb strength criterion. With the increase of curing time, the friction angle (φ_b) was exponentially decreased but the cohesive (c_b) experienced an exponential increase. There is also an obvious secondary elastic strengthening stage identified in the stress-strain curves under a higher σ_3/UCS (≥20%).

- The established damage constitutive model can accurately describe the triaxial stress-strain relationships with and without the secondary elastic strengthening stage of CPB under different curing time. The theoretical curves agreed favorably with the experimental results.

Declaration of Competing Interest

The authors declare that they have no known competing financial interests or personal relationships that could have appeared to influence the work reported in this paper.

Acknowledgments

This work was conducted with supports from the National Natural Science Foundation of China (Grant No. U1602232), Liaoning Science and Technology Project (2019JH2/10100035). Also, the authors would like to thank PhD. Haiqiang Jiang for supplying the silica tailings and tested mold.

References

[1] D. Ma, H. Duan, J. Liu, X. Li, Z. Zhou, The role of gangue on the mitigation of mining-induced hazards and environmental pollution: An experimental investigation, Sci. Total Environ. 664 (2019) 636-448. https://doi.org/10.1016/j.scitotenv.2019.02.059.

[2] Q. Chen, Q. Zhang, C. Qi, A. Fourie, C. Xiao, Recycling phosphogypsum and construction demolition waste for cemented paste backfill and its environmental impact, J. Clean. Prod. 186 (2018) 418-429. https://doi.org/10.1016/j.jclepro.2018.03.131.

[3] D. Deng, L. Liu, Z. Yao, K.I. Song, D. Lao, A practice of ultra-fine tailings disposal as filling material in a gold mine, J. Environ. Manage. 196 (2017) 100-109. https://doi.org/10.1016/j.jenvman.2017.02.056.

[4] A.J. Bull, M. Fall, Curing temperature dependency of the release of arsenic from cemented paste backfill made with Portland cement, J. Environ. Manage. 269 (2020) 110772. https://doi.org/10.1016/j.jenvman.2020.110772.

[5] S.K. Behera, C.N. Ghosh, D.P. Mishra, P. Singh, K. Mishra, J. Buragohain, P.K. Mandala, Strength development and microstructural investigation of lead-zinc mill tailings based paste backfill with fly ash as alternative binder, Cem. Concr. Compos. 109 (2020) 103553. https://doi.org/10.1016/j.cemconcomp.2020.103553.

[6] F. Zhang, W. Liu, L. Shen, Damage constitutive model for cemented paste backfill after mixing waste rock, World Automation Congress (WAC), IEEE, 2012, Puerto Vallarta, Mexico.

[7] B. Tu, L. Liu, K. Cheng, B. Zhang, K. Song, A constitutive model for cemented tailings backfill under uniaxial compression, Front. Physics. 8 (2020) 173. https://doi.org/10.3389/fphy.2020.00173.

[8] K. Cheng, B. Tu, L. Liu, B. Zhang, H. Qiu, Damage strengthening constitutive model of cemented paste backfill, Adv. Civ. Eng. 10 (2021) 5593983. https://doi.org/10.1155/2021/5593983.

[9] R. Gao, K. Zhou, C. Yang, Damage mechanism of composite cemented backfill based on complex defects influence, Materialwiss. Werkstofftech. 48 (9) (2017) 893-904. https://doi.org/10.1002/mawe.201600722.

[10] J. Qiu, L. Yang, J. Xing, X. Sun, Analytical solution for determining the required strength of mine backfill based on its damage constitutive model, Soil Mech. Found. Eng. 54 (6) (2018) 371-376. https://doi.org/10.1007/s11204-018-9483-7.

[11] J. Wang, J. Fu, W. Song, Y. Zhang, Y. Wang, Mechanical behavior, acoustic emission properties and damage evolution of cemented paste backfill considering structural feature, Constr. Build. Mater. 261 (2020) 119958. https://doi.org/10.1016/j.conbuildmat.2020.119958.

[12] J. Wang, J. Fu, W. Song, Y. Zhang, S. Wu, Acoustic emission characteristics and damage evolution process of layered cemented tailings backfill under uniaxial compression, Constr. Build. Mater. 295 (2021) 123663. https://doi.org/10.1016/j.conbuildmat.2021.123663.

[13] J. Fu, J. Wang, W. Song, Damage constitutive model and strength criterion of cemented paste backfill based on layered effect considerations, J. Mater. Res. Technol-JMRT. 9 (3) (2020) 6073-6084. https://doi.org/10.1016/j.jmrt.2020.04.011.

[14] R. Gao, K. Zhou, J. Li, Research of the mechanisms of backfill formation and damage, Mater. Tehnol. 52 (2018) 163-169. https://doi:10.17222/mit.2017.070.

[15] Z. Wang, P. Yang, W. Lyu, G. Yu, C. Yang, Study of the backfill confined consolidation law and creep constitutive model under high stress, Geotech. Test. J. 41 (2) (2018) 20160263. https://doi:10.1520/GTJ20160263.

[16] Q. Sun, B. Li, S. Tian, C. Cai, Y. Xia, Creep properties of geopolymer cemented coal gangue-fly ash backfill under dynamic disturbance, Constr. Build. Mater. 191 (2018) 644-654. https://doi.org/10.1016/j.conbuildmat.2018.10.055.

[17] Y. Guo, H. Ran, G. Feng, X. Du, Y. Zhao, W. Xie, Deformation and instability properties of cemented gangue backfill column under step-by-step load in constructional backfill mining, Environ. Sci. Pollut. Res. 8 (2021) 1-17. https://doi.org/10.1007/s11356-021-15638-z.

[18] L. Zhang, H. Wang, A. Wu, B. Klein, X. Zhang, A constitutive model for thixotropic cemented tailings backfill pastes, J. Non-Newton. Fluid Mech. 295 (2021) 104548. https://doi.org/10.1016/j.jnnfm.2021.104548.

[19] G. Lu, M. Fall, Z. Yang, An evolutive bounding surface plasticity model for early-age cemented tailings backfill under cyclic loading, Soil Dyn. Earthq. Eng. 117 (2019) 339-356. https://doi.org/10.1016/j.soildyn.2018.11.017.

[20] C. Liang, M. Fall, A coupled thermo–hydro-mechanical-chemical model for underground cemented tailings backfill, Tunn. Undergr. Space Technol. 50 (2015) 396-414. https://doi.org/10.1016/j.tust.2015.08.014.

[21] G. Lu, M. Fall, Modelling blast wave propagation in a subsurface geotechnical structure made of an evolutive porous material, Mech. Mater. 108 (2017) 21-39. https://doi.org/10.1016/j.mechmat.2017.03.003.

[22] L. Cui, M. Fall, Mathematical modelling of cemented tailings backfill: a review, Int. J. Min. Reclam. Env. 42 (3) (2018) 558-583. https://doi.org/10.1080/17480930.2018.1453320.

[23] M. Fall, T. Belem, S. Samb, M. Benzaazoua, Experimental characterization of the stress–strain behaviour of cemented

paste backfill in compression, J. Mater. Sci. 42 (11) (2007) 3914-3922. https://doi.org/10.1007/s10853-006-0403-2.

[24] Q. Liu, D. Liu, Y. Tian, X. Liu, Numerical simulation of stress-strain behaviour of cemented paste backfill in triaxial compression, Eng. Geol. 231 (2017) 165-175. https://doi.org/10.1016/j.enggeo.2017.10.021.

[25] J. Fu, W. Song, Y. Tan, Study on microstructural evolution and strength growth and fracture mechanism of cemented paste backfill, Adv. Mater. Sci. Eng. 2016 (2016) 1-13. https://doi.org/10.1155/2016/8792817.

[26] L. Yang, W. Xu, E. Yilmaz, Q. Wang, J. Qiu, A combined experimental and numerical study on the triaxial and dynamic compression behavior of cemented tailings backfill, Eng. Struct. 219 (2020) 110957. https://doi.org/10.1016/j.engstruct.2020.110957.

[27] K. Fang, M. Fall, Effects of curing temperature on shear behaviour of cemented paste backfillrock interface, Int. J. Rock Mech. Min. 112 (2018) 184-192. https://doi.org/10.1016/j.ijrmms.2018.10.024.

[28] K. Fang, M. Fall, Chemically induced changes in the shear behaviour of interface between rock and tailings backfill undergoing cementation, Rock Mech. Rock. Eng. 52 (9) (2019) 3047-3062. https://doi.org/10.1007/s00603-019-01757-0.

[29] K. Fang, M. Fall, Shear behavior of the interface between rock and cemented backfill: effect of curing Stress, drainage condition and backfilling rate, Rock Mech. Rock Eng. 53 (2020) 325-336. https://doi.org/10.1007/s00603-019-01909-2.

[30] ASTM D2487-17e1, Standard Practice for Classification of Soils for Engineering Purposes (Unified Soil Classification System). ASTM International, 2017, West Conshohocken, PA. https://doi.org/10.1520/D2487-17E01.

[31] Z. Xiu, S. Wang, Y. Ji, F. Wang, F. Ren, V. Nguyena, The effects of dry and wet rock surfaces on shear behavior of the interface between rock and cemented paste backfill, Powder Technol. 381 (2021) 324-337. https://doi.org/10.1016/j.powtec.2020.11.053.

[32] Z. Xiu, S. Wang, Y. Ji, F. Wang, F. Ren, V. Nguyena, Loading rate effect on the uniaxial compressive strength (UCS) behavior of cemented paste backfill (CPB), Constr. Build. Mater. 271 (2020) 121526. https://doi.org/10.1016/j.conbuildmat.2020.121526.

[33] Z. Xiu, S. Wang, Y. Ji, F. Wang, F. Ren, Experimental investigation on liquefaction and post-liquefaction deformation of stratified saturated sand under cyclic loading, Bull. Eng. Geol. Environ. 79 (2020) 2313-2324. https://doi.org/10.1007/s10064-019-01696-8.

[34] C. Li, C. Li, R. Zhao, L. Zhou, A strength criterion for rocks, Mech. Mater. 154 (3) (2021) 1-9. https://doi.org/10.1016/j.mechmat.2020.103721.

[35] W. Weibull, A statistical distribution function of wide applicability, ASME J. Appl. Mech. 18 (1951) 293-297. https://doi.org/10.1093/qjmam/6.4.453.

[36] F. Wang, K. Xia, W. Yao, S. Wang, C. Wang, Z. Xiu, Slip behavior of rough rock discontinuity under high velocity

impact: Experiments and models, Int. J. Rock Mech. Min. Sci. 144 (2021) 104831. https://doi.org/10.1016/j.ijrmms.2021.104831.

[37] L. Xiang, W. Cao, Y. Su, A statistical damage constitutive model for softening behavior of rocks, Eng. Geol. 143-144 (2012) 1-17. https://doi.org/10.1016/j.enggeo.2012.05.005.